chemistry

MDPI

*Article*

# Substituent-Tuned Quinone Electron Traps for High-Energy-Density Capacitive Storage in PMMA Dielectrics

**Zhiwei Wang [1,2], Yuanqi Wang [1,2], Jiahong Li [1,2], Xin Gao [1,2,*], Chenyi Li [1,2,*] and Yang Liu [1,2]**

[1] State Key Laboratory of Material Processing and Die & Mould Technology, School of Materials Science and Engineering, Huazhong University of Science and Technology, Wuhan 430074, China; 18216291986@163.com (Z.W.); yqwang624@hust.edu.cn (Y.W.); lijhong@hust.edu.cn (J.L.); yliu1319@hust.edu.cn (Y.L.)

[2] Guangdong Provincial Key Laboratory of Manufacturing Equipment Digitization, Guangdong HUST Industrial Technology Research Institute, Dongguan 523808, China

* Correspondence: gao_xin@hust.edu.cn (X.G.); chenyi_li@hust.edu.cn (C.L.)

**Abstract**

Poly(methyl methacrylate) (PMMA) is an attractive linear dielectric for capacitive energy storage, but high-field carrier injection and transport cause conduction loss that limits energy density and efficiency. Here, three structurally related quinone acceptors, tetramethyl-1,4-benzoquinone (TDQ), tetrachloro-1,4-benzoquinone (TCQ), and tetrafluoro-1,4-benzoquinone (TFQ), are incorporated into PMMA via solution casting to construct all-organic composites with substituent-regulated electron traps. Density functional theory calculations reveal that peripheral substitution modulates frontier orbitals and electrostatic environments; TCQ has the deepest lowest unoccupied molecular orbital (LUMO) and the largest LUMO offset relative to PMMA. Combined TSDC, hopping-conduction and Weibull analyses confirm that TCQ most effectively suppresses leakage current and enhances breakdown strength. The optimized PMMA/TCQ film achieves a recoverable energy density of 17.81 J $cm^{-3}$ at 950 MV $m^{-1}$ with an efficiency of 84.08% and 9.83 J $cm^{-3}$ at 700 MV $m^{-1}$ with an efficiency of 90.83% at room temperature, with stable cycling and good spatial uniformity. This work proves that substituent engineering of quinone acceptors is an effective molecular strategy to confine carrier transport and improve the energy-storage performance of PMMA dielectrics.

**Keywords:** polymer dielectric; quinone acceptor; charge trapping; conduction loss; capacitive energy storage

Check for updates

Academic Editor: Michael Lyons

Received: 22 October 2026
Revised: 7 November 2026
Accepted: 9 November 2026
Published: 21 November 2026

**Copyright:** © 2026 by the authors. Licensee MDPI, Basel, Switzerland. This article is an open access article distributed under the terms and conditions of the Creative Commons Attribution (CC BY) license.

## 1. Introduction

Polymer dielectric capacitors are important components in pulsed-power systems and power electronics because of their rapid charge–discharge capability, high power density, and processing flexibility [1–7]. The increasing demand for compact devices has driven efforts to improve energy density while maintaining high discharge efficiency and reliable electrical insulation.

Poly(methyl methacrylate) (PMMA) is a representative linear polar polymer featuring favorable insulating performance, low dielectric loss, and convenient solution processability. Its side-chain ester groups enable dipolar polarization, which underpins its capacitive energy-storage function. Nevertheless, severe carrier injection and long-range carrier transport under high electric fields generate substantial leakage current, which induces energy dissipation, degrades discharge efficiency, and raises the risk of electrical breakdown [8–10].

Therefore, suppressing conduction loss is essential for unlocking the full energy-density potential of PMMA.

Charge-trap engineering provides a molecular approach to restricting carrier transport [11–17]. Yuan et al. demonstrated that high-electron-affinity ($E_a$) molecular semiconductors can capture electrons and suppress charge injection and conduction in polymer dielectrics [18]. Zhang et al. incorporated bulky electron-deficient units to suppress conduction and relaxation losses [19], while He et al. demonstrated improved dielectric and energy-storage properties through charge-trapping copolymer structures [20]. Collectively, these works validate the tight correlation between molecular charge regulation and capacitive response and lay a rational foundation for selecting electron-accepting additives for the PMMA matrix [6,21].

The trapping performance of a molecular trap is governed jointly by its intrinsic electronic structure and local chemical environment within the polymer host. Previous studies on polystyrene dielectrics have verified substituent-tunable electronic effects of molecular acceptors [6,20], and polyetherimide-based systems further highlight how trap energetics, molecular conformation and interfacial interactions modulate carrier migration [21–23]. In particular, Lin et al. introduced tetrabromo-1,4-benzoquinone (TBQ) into polyetherimide (PEI) and demonstrated the effectiveness of molecular charge trapping in improving high-temperature capacitive energy storage [15]. However, although the effectiveness of molecular trapping has been established, a systematic understanding of how different substituents within the same quinone framework influence charge-trapping characteristics and high-field dielectric performance in a fixed polymer matrix remains limited. Such a comparison is essential for distinguishing substituent-dependent electronic effects from the influence of different molecular backbones and polymer matrices. These advances inspire us to compare a series of structurally analogous acceptors dispersed in the same PMMA matrix. Substituted parabenzoquinones constitute an ideal molecular platform, as their conjugated quinone backbone supports electron uptake and peripheral substituents permit deliberate tuning of electronic characteristics [24]. This framework allows us to directly link additive chemical structure to leakage-current suppression.

Herein, TDQ, TCQ, and TFQ are incorporated into PMMA to fabricate all-organic dielectric films relying on substituent-regulated molecular charge trapping. By maintaining the same quinone molecular framework and PMMA matrix while varying only the peripheral substituents, we establish a controlled comparative system to investigate the relationship between molecular substitution, charge-trapping characteristics, and high-field electrical performance. We leverage the energy offset between quinone acceptors and the polymer matrix to facilitate electron capture and hinder carrier transport. Among the three candidates, TCQ possesses the lowest calculated unoccupied molecular orbital (LUMO), indicative of superior electron-accepting capability. The optimized PMMA/TCQ film delivers a recoverable energy density of 9.83 J $cm^{-3}$ with a discharge efficiency of 90.83% at 700 MV $m^{-1}$ under room-temperature conditions. By correlating molecular electronic structure, charge-trapping behavior and high-field conduction, this work establishes a clear design guideline to upgrade the energy-storage performance of PMMA-based dielectrics.

## 2. Materials and Methods

### *2.1. Materials*

PMMA (weight-average molecular weight, Mw = 90,000 g $mol^{-1}$) was purchased from PolyK Technologies (State College, PA, USA). TDQ (99.99%), TCQ (99.99%), and TFQ (99.99%) were obtained from Sigma-Aldrich (St. Louis, MO, USA). N-methyl-2-pyrrolidone

(NMP, anhydrous, 99.5%) was purchased from Sigma-Aldrich. All reagents and solvents were used as received.

### *2.2. Preparation of Composite Films*

PMMA-based composite films were fabricated by solution casting. First, PMMA was dissolved in NMP at a concentration of 40 mg $mL^{-1}$ under stirring at 60 °C for 24 h. A predetermined amount of TDQ, TCQ, or TFQ was dissolved in NMP and subsequently mixed with the PMMA solution. The mixture was stirred at 40 °C for 2 h to obtain a homogeneous casting solution.

The additive loadings were set to 0.25, 0.50, 0.75, 1.00, 1.25, 1.50, 1.75, and 2.00 wt%. The composite films were denoted PMMA/TDQ-x, PMMA/TCQ-x, and PMMA/TFQ-x, where x represents the mass fraction of the quinone additive. The composite films used for experimental characterization in Sections 3.1–3.4 and Figures S2–S6 contain 1.00 wt% of the corresponding quinone additive.

The casting solution was degassed under vacuum to eliminate entrapped air bubbles and poured onto pre-cleaned glass substrates for solution casting. Wet films were first dried at 80 °C for 6 h to slowly evaporate most solvent, followed by vacuum drying at 100 °C for 4 h to eliminate residual solvent. After naturally cooling to room temperature, the solid films were peeled off from the glass substrates and stored in a dry cabinet prior to characterization. Neat PMMA films were prepared under identical processing conditions as the control sample. The final thickness of all obtained films was controlled at approximately 6 μm.

### *2.3. Structural and Thermal Characterization*

Fourier-transform infrared (FTIR) spectra were collected using an INVENIO-S (Bruker, Billerica, MA, USA) equipped with an attenuated total reflectance accessory. Film specimens were measured directly over a wavenumber range of 4000–400 $cm^{-1}$ at a resolution of 4 $cm^{-1}$. Ultraviolet–visible (UV–vis) absorption spectra were recorded using a SolidSpec-3700 (Shimadzu, Kyoto, Japan) over a wavelength range of 200–800 nm. The optical bandgap was estimated using the Tauc plot method by plotting $(\alpha h\nu)^2$ against photon energy $h\nu$, where $\alpha$ is the absorption coefficient. The optical bandgap was obtained by extrapolating the linear region near the absorption edge to the photon-energy axis.

### *2.4. Electrical Characterization*

For all electrical and dielectric measurements, Au electrodes (50 nm) were sputtered onto both sides of the films using an automated sputter coater (Q150RS, Quorum, Laughton, UK). Dielectric spectroscopy over the frequency range of 100 Hz to 1 MHz was performed using an E4980A precision LCR meter (Keysight Technologies, Santa Rosa, CA, USA). The reported dielectric constant refers to relative permittivity, while dielectric loss refers to the dielectric loss tangent, defined as the ratio of the dielectric loss factor to relative permittivity. Both quantities are dimensionless. Temperature-dependent dielectric properties were also measured by an E4980A precision LCR meter in a temperature-controlled system (Beijing Hua Ce Testing Instrument, Beijing, China) at a heating rate of 2 °C $min^{-1}$. Electric-field-dependent leakage current density was recorded with an electrometer (Keithley 6517B, Keithley Instruments, Cleveland, OH, USA) equipped with a high-voltage amplifier (Trek 610C, Trek Inc., Medina, NY, USA), while temperature was controlled using an oven (Sun Electronics, Seoul, Republic of Korea). TSDC measurements were carried out on a Keithley 6517B electrometer coupled to a temperature-control system (Beijing Hua Ce Testing Instrument). In a typical TSDC experiment, the samples were polarized at 70 °C under a DC field of 50 MV $m^{-1}$ for 30 min. The specimens were then cooled to 30 °C at

20 °C min$^{-1}$ while maintaining the applied field. After thermal stabilization at 30 °C, the field was removed and the electrodes were short-circuited. The depolarization current was subsequently recorded during heating from 30 °C to 150 °C at 3 °C min$^{-1}$. For dielectric spectroscopy, leakage-current measurements and TSDC tests, the electrode diameter was 4 mm. Weibull statistics for breakdown strength were obtained from 12 specimens using a high-voltage amplifier (Trek 610C) with a DC voltage ramp rate of 500 V s$^{-1}$ and the electrode diameter of the sample was 1 mm. Unipolar *D*–*E* loops were measured using a modified Sawyer–Tower circuit under a unipolar waveform at 100 Hz and the electrode diameter used in this test was 2 mm. The charging and discharged energy densities were calculated by integrating the electric field with respect to electric displacement along the corresponding charging and discharging branches of the *D*–*E* loops. The charge–discharge efficiency was determined as the ratio of the discharged energy density to the charging energy density, multiplied by 100%. In the breakdown strength and *D*–*E* loops tests, the samples were immersed in methylphenyl silicone oil (Shin Etsu, Tokyo, Japan) to prevent surface flashover. The oil temperature was regulated using a hot plate in conjunction with a thermocouple feedback controller. The rapid discharge tests proceeded through a dielectric charging and discharging system (Beijing Hua Ce Testing Instrument) with a load resistor of 100 kΩ.

### *2.5. Calculation of the Weibull Breakdown Strength*

Breakdown behaviour is analysed using a two-parameter Weibull statistics model [25,26], expressed as

$$P(E) = 1 - \exp\left(-(E/E_b)^{\beta}\right) \quad (1)$$

where $P(E)$ is the cumulative probability of electrical failure and $E$ is the measured breakdown field; the scale parameter $E_b$ is defined as the Weibull breakdown strength corresponding to a 63.2% failure probability, whereas the shape parameter $\beta$ reflects the scatter of the experimental data.

### *2.6. Calculation of the Hopping Distance*

The current density generated by hopping conductance can be expressed as [27,28]

$$J(E,T) = 2ne\lambda v * \exp\left(-\left(\frac{E_a}{K_bT}\right)\right) * \sinh\left(\frac{\lambda eE}{2K_bT}\right) \quad (2)$$

where $n$ is the carrier concentration, $\lambda$ is the hopping distance, $v$ is the attempt-to-escape frequency, $e$ the charge of the carriers, $E_a$ characterizes the activation energy associated with hopping conductance, $T$ signifies the absolute temperature, $K_b$ is the Boltzmann constant and $E$ represents the electric field strength.

At a given temperature, the above equation can be simplified as [29,30]

$$J(E) = J_0 * \sinh(\alpha E) \quad (3)$$

where $J_0$ and $\alpha$ represent two lumped parameters. Consequently, we can model the ln($J$)-versus-$E$ curves using hopping conduction and determine the hopping distance, which is included in parameter $\alpha$.

### *2.7. Density Functional Theory (DFT) and Time-Dependent DFT Calculations*

The structural optimizations of quinone molecules and PMMA/quinone model complexes were carried out at the B3LYP/6-31G(d,p) level within the Gaussian program package [31,32]. The electronic energy-level comparison was performed using representative molecular models of PMMA and the three quinone derivatives. The relative LUMO energy offset was defined as

$$\Delta E_{\mathrm{LUMO}}^{\mathrm{DFT}} = \varepsilon_{\mathrm{LUMO}}^{\mathrm{PMMA}} - \varepsilon_{\mathrm{LUMO}}^{\mathrm{quinone}}$$

where the two terms represent the calculated LUMO energies of the PMMA reference model and the corresponding quinone molecule, respectively. These orbital energy differences were employed as qualitative indicators of the relative electron-accepting characteristics rather than quantitative predictions of solid-state trap activation energies.

Molecular electrostatic potential and electron localization function (ELF) analyses were subsequently performed on the optimized geometries. Time-dependent density functional theory (TDDFT) calculations adopting the CAM-B3LYP/6-31G(d,p) scheme were implemented to obtain the electronic transition information required for charge-transfer spectrum (CTS) analysis, and the CTS was further computed using Multiwfn [33]. The long-range corrected CAM-B3LYP functional is well suited for describing charge-transfer excitations and long-range electronic couplings compared with conventional B3LYP.

### *2.8. Calculation of TSDC-Derived Trapped Energy Levels and Depolarization Charge*

The trapped energy levels associated with the TSDC peak were evaluated using the peak-width method:

$$E_{TSDC} = \frac{2.47 K_b T_p^2}{\Delta T} \quad (4)$$

where $T_p$ denotes the peak-current temperature, $\Delta T$ is the temperature difference for the half-height peak, and $K_b$ is the Boltzmann constant.

The integrated depolarization charge was calculated by integrating the TSDC over the selected temperature interval:

$$Q = \int_{t_0}^{t_1} I_{corr}(t)\, dt = \frac{1}{\beta} \int_{T_0}^{T_1} I_{corr}(T)\, dT \quad (5)$$

where $Q$ is the integrated depolarization charge, $I_{corr}(T)$ is the baseline-corrected depolarization current, and $\beta$ is the constant heating rate of 3 °C min$^{-1}$.

## 3. Results

### *3.1. Molecular Design and Charge-Trapping Mechanism*

The electron-accepting character of the quinone framework provides a viable molecular route to introduce charge traps into PMMA. Its conjugated carbonyl backbone readily accepts electrons, while peripheral substitution offers a straightforward handle to tailor electronic properties. With this rationale, TDQ, TCQ, and TFQ were selected as molecular additives bearing methyl, chloro, and fluoro substituents, respectively (Figure 1a). This set of structurally similar acceptors enables us to interrogate how substituent-modulated energy-level alignment governs electron capture and carrier transport within the PMMA matrix.

Frontier orbital analysis reveals the key electronic states underlying this design strategy (Figure 1b). Unoccupied states capable of accommodating excess electron density primarily localize on the quinone core and carbonyl groups. Substitution alters both the spatial distribution and energetic position of these orbitals. Electrostatic potential maps and area histograms further capture accompanying shifts in the local electrostatic environment (Figure 1c–e). TCQ produces a broadly distributed surface potential histogram, whereas TDQ and TFQ feature sharper, concentrated positive potential peaks. These two types of descriptors offer complementary insights. Electrostatic potential describes the near-molecule spatial environment, while frontier orbital energies reflect the energetic accessibility of electronic states. Combined, these results confirm that the three additives are not electronically equivalent, despite sharing the same quinone scaffold.

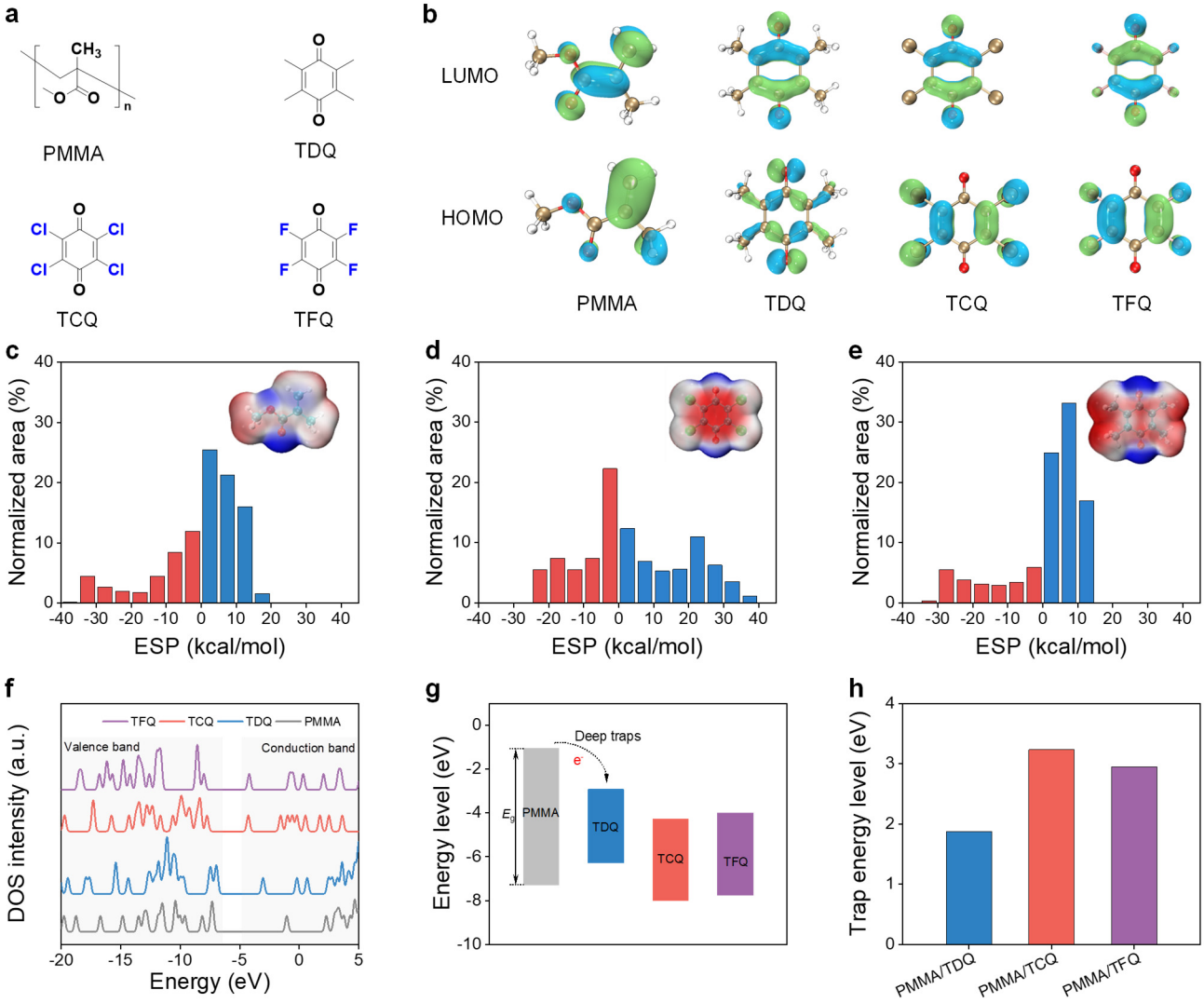



**Figure 1.** Molecular structures, frontier orbital distributions, electrostatic potential (ESP) characteristics, density of states (DOS), and trap energy level analysis of PMMA, TDQ, TCQ, and TFQ. (**a**) Chemical structures of PMMA matrix and three quinone fillers (TDQ, TCQ, TFQ); (**b**) highest occupied molecular orbital (HOMO) and LUMO isosurfaces of four molecules; (**c**–**e**) ESP distribution histograms and ESP isosurfaces for TDQ, TCQ, and TFQ, respectively; (**f**) calculated DOS spectra of PMMA and three composite systems; (**g**) schematic illustration of deep electron trap formation induced by quinone fillers in PMMA matrix; (**h**) comparison of calculated LUMO energy offsets between PMMA and the three quinone additives.

Density-of-states profiles and energy-level alignment further differentiate the three acceptors (Figure 1f,g). All three molecules carry LUMO energies lower than that of the neat PMMA reference. Among them, TCQ possesses the deepest LUMO and the largest LUMO offset relative to PMMA, followed sequentially by TFQ and TDQ (Figure 1h). Electrons trapped in these lower-energy acceptor states become unavailable for long-range charge transport, which makes TCQ the most promising candidate for efficient electron capture within this series.

CTS calculations were performed to resolve electronic redistribution at the PMMA–quinone interface (Figure 2a). The dominant charge-transfer band between two PMMA fragments serves as a baseline. After incorporating quinone additives, the main PMMA-to-acceptor forward charge-transfer peak weakens [9]. TCQ gives the lowest forward transfer peak intensity, indicating suppressed forward charge-transfer excitation. Meanwhile, the reverse transfer component remains substantial in the PMMA/TCQ system. This observa-

tion demonstrates that chlorine substitution reshapes the balance between forward and reverse charge-transfer excitations. Such spectral distinctions complement the energy-level comparison in Figure 1 and indicate that peripheral substitution modulates the charge-transfer excitation characteristics between PMMA and the embedded acceptors. Notably, CTS reflects the electronic excitation characteristics of the molecular systems rather than directly quantifying carrier-transfer rates under applied electric fields. Therefore, these results provide further insight into the substituent-dependent modulation of molecular electronic structure and charge-transfer characteristics.

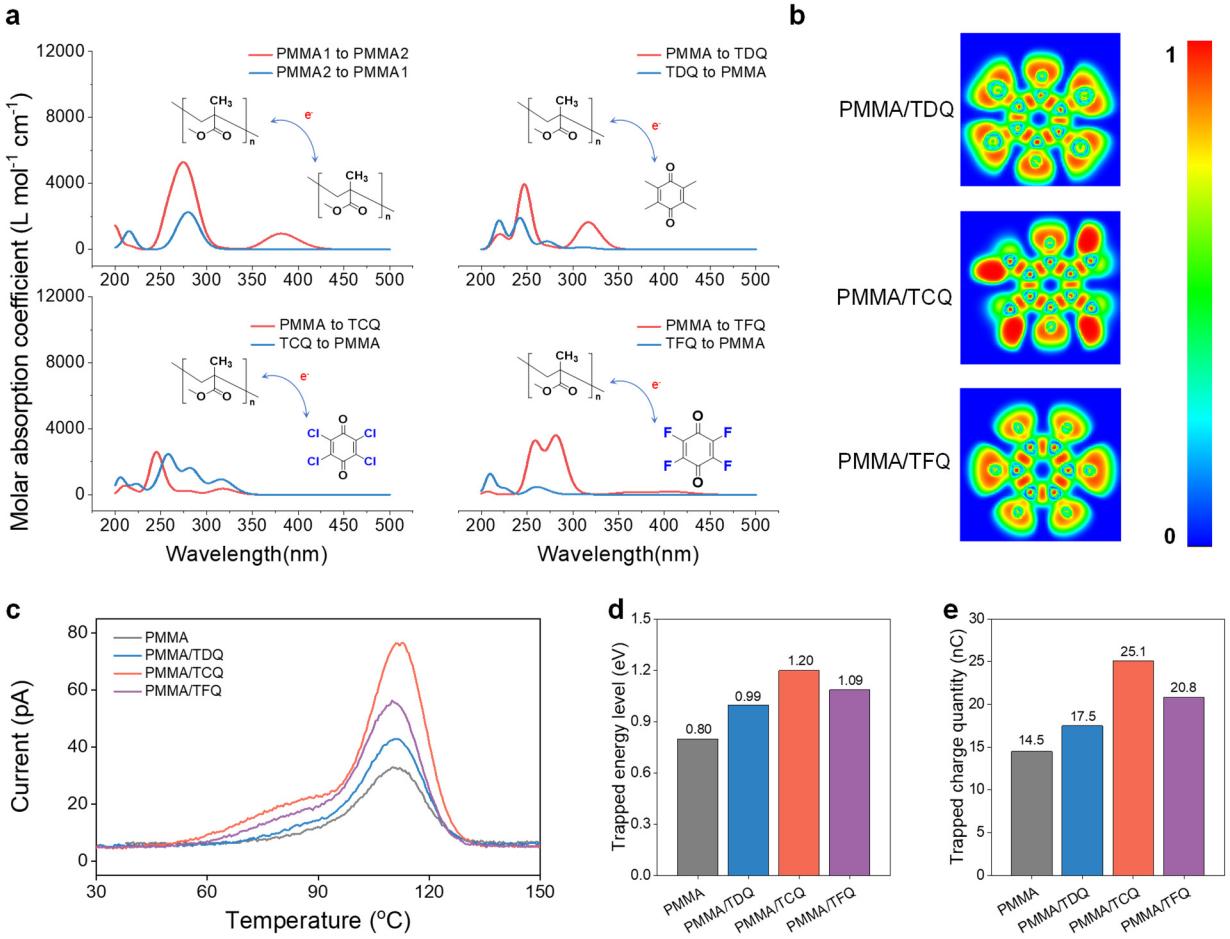



**Figure 2.** Photoinduced electron transfer behavior, ELF analysis, and TSDC characterization of PMMA-based composite films. (**a**) Molar absorption coefficient spectra for electron transfer processes between PMMA segments and quinone molecules (PMMA → PMMA, PMMA → TDQ, PMMA → TCQ, PMMA → TFQ and reverse processes); (**b**) ELF maps of PMMA/TDQ, PMMA/TCQ, and PMMA/TFQ systems; (**c**) TSDC curves of neat PMMA and three composite films tested from 30 to 150 °C; (**d**) trap energy levels calculated from TSDC curves; (**e**) statistical trapped charge quantity of each sample derived from TSDC integration.

ELF analysis visualizes the spatial confinement of electron pairs (Figure 2b). The color bar ranges from blue (ELF = 0) to red (ELF = 1), where higher ELF values correspond to stronger localization of electron pairs [9]. Compared with PMMA/TDQ and PMMA/TFQ, PMMA/TCQ shows extended red ELF signals surrounding the quinone periphery. These high-ELF domains mark tightly confined bound electron pairs localized on the additive. ELF maps together with orbital calculations therefore paint a consistent picture for TCQ. Specifically, ELF reveals the localized distribution of occupied electrons, whereas the low-lying LUMO states indicate favorable electron-accepting characteristics. These complementary

electronic-structure features provide a molecular-level basis for understanding the potential charge-trapping behavior of TCQ.

To experimentally verify the charge-trapping behavior, we carried out thermally stimulated depolarization current (TSDC) measurements on neat PMMA and the three composite films (Figure 2c–e). All samples show a major depolarization peak near 120–130 °C, and peak intensity follows the trend PMMA < PMMA/TDQ < PMMA/TFQ < PMMA/TCQ. Fitting of TSDC curves yields apparent trap depths of 0.80, 0.99, 1.09, and 1.20 eV for PMMA, PMMA/TDQ, PMMA/TFQ, and PMMA/TCQ, respectively (Figure 2d). The total depolarization charge, obtained via integration of TSDC profiles, increases from 14.5 nC for neat PMMA to 17.5, 20.8, and 25.1 nC for PMMA/TDQ, PMMA/TFQ, and PMMA/TCQ (Figure 2e). PMMA/TCQ simultaneously delivers the deepest apparent trap and the largest depolarization charge. This experimental evidence confirms that TCQ-derived traps effectively immobilize charge carriers and suppress their migration, matching the predictions from our proposed trapping mechanism. The TSDC response of PMMA may involve both dipolar relaxation and trapped-charge release. Since all samples were tested under identical conditions, neat PMMA serves as a reference. The increased depolarization charge, comparable dielectric responses, and consistent leakage-current trends support the contribution of substituent-dependent charge trapping. Nevertheless, possible contributions from dipolar relaxation should be considered, and the extracted energies are therefore regarded as apparent activation energies.

### *3.2. Structural Characterization and High-Field Electrical Behavior*

We first used FTIR spectroscopy to check the chemical compatibility between PMMA and quinone additives. As shown in Figure S2, the characteristic C=O and C–O–C stretching bands of PMMA exhibit no appreciable shifts or broadening after the incorporation of quinone additives, and no new absorption bands are observed. These results indicate the absence of significant polymer–additive interactions detectable by FTIR. UV–vis spectra show only mild narrowing of the optical bandgap upon quinone doping (Figures S3–S6).

Frequency-dependent dielectric measurements were then collected. At room temperature across 100 Hz–1 MHz, all three composites exhibit higher permittivity than neat PMMA (Figures 3a and S7–S9). The permittivity reaches ~4.2 at 1 kHz, versus ~3.6 for pristine PMMA. Permittivity gradually declines with rising frequency, consistent with the fading contribution of slow polarization processes at faster alternating fields. Notably, permittivity differences among PMMA/TDQ, PMMA/TCQ, and PMMA/TFQ remain modest. This implies similar low-field polarization responses, even though their acceptor energy levels differ markedly. Dielectric loss decreases with frequency and stays within a narrow, comparable range across all four samples (Figures 3b and S7–S9). In other words, molecular doping does not introduce obvious extra dielectric loss under low fields.

Temperature-dependent dielectric spectra were measured from 30 to 100 °C. Permittivity rises alongside temperature, accompanied by a moderate increase in dielectric loss (Figures 3c,d and S10–S12). This trend aligns with thermally activated segmental motion and polarization relaxation. Over the tested temperature window, composite loss spectra remain close to that of neat PMMA, confirming that the additives barely perturb the intrinsic loss characteristics of the host polymer.

Leakage current measurements at room temperature produce far clearer differentiation between the three doped systems (Figure 3e). Current density rises with electric field for every sample, yet at identical field strengths, the magnitude obeys PMMA > PMMA/TDQ > PMMA/TFQ > PMMA/TCQ. Near 300 MV $m^{-1}$, the leakage current density of PMMA/TCQ falls more than one order of magnitude below that of neat PMMA. This field-dependent divergence directly supports our hypothesis that acceptor states restrict mobile carrier transport, standing in sharp contrast to the small permittivity differences observed under low fields.

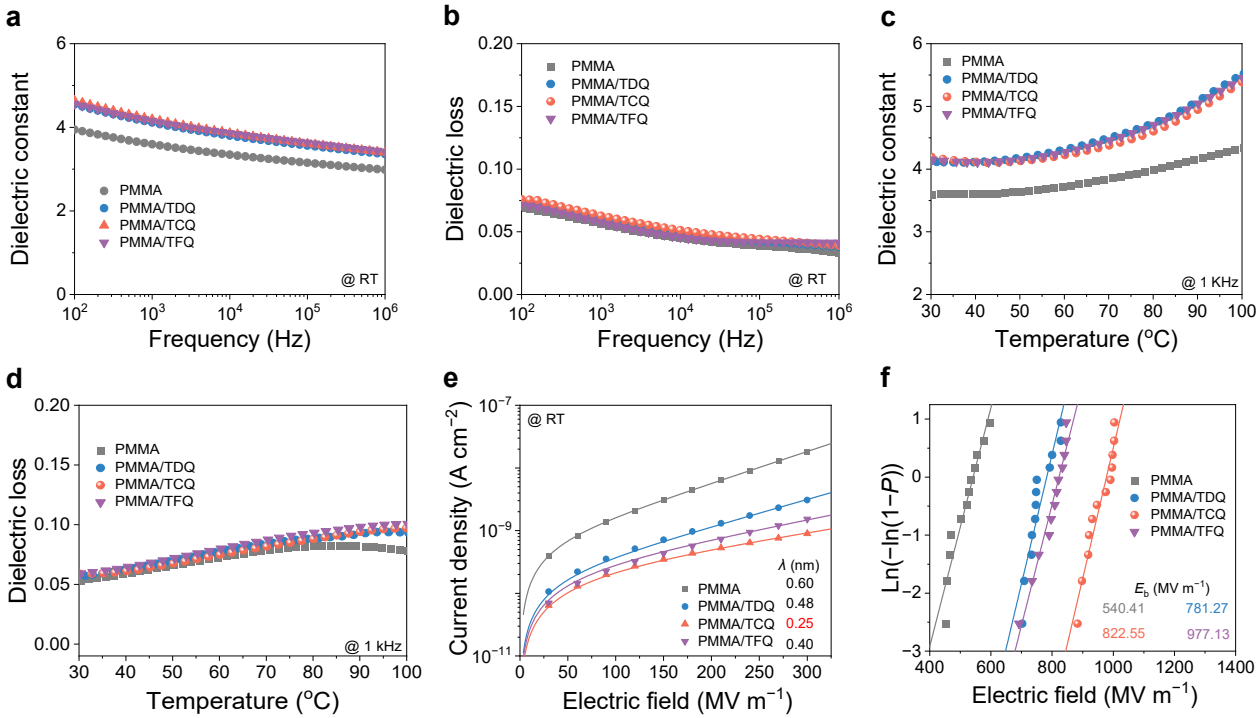



**Figure 3.** Dielectric properties, leakage current, and breakdown strength of neat PMMA, PMMA/TDQ, PMMA/TCQ, and PMMA/TFQ composite films. (**a**) Frequency-dependent dielectric constant at room temperature; (**b**) frequency-dependent dielectric loss at room temperature; (**c**) temperature-dependent dielectric constant measured at 1 kHz; (**d**) temperature-dependent dielectric loss measured at 1 kHz; (**e**) leakage current density as a function of applied electric field at room temperature; (**f**) Weibull distribution plots of breakdown strength for all film samples.

We further fitted current–field curves using a hopping conduction model at 25 °C. The extracted effective hopping distances are approximately 0.60, 0.48, 0.25, and 0.40 nm for PMMA, PMMA/TDQ, PMMA/TCQ, and PMMA/TFQ, respectively. PMMA/TCQ has the smallest hopping distance, which correlates well with its suppressed leakage current. A shorter effective hopping distance indicates a smaller characteristic length associated with field-assisted hopping within the adopted conduction model. The consistent ranking between leakage current and fitted hopping distance validates our molecular design strategy for carrier suppression. To further examine possible charge-conduction mechanisms, the leakage-current data were also analyzed using Schottky emission and Poole–Frenkel models. These analyses provide complementary information to the hopping conduction model.

Reduced leakage conduction is expected to improve high-field insulation. We quantified breakdown performance via Weibull statistics (Figures 3f and S13–S15). The characteristic breakdown strengths of pristine PMMA, PMMA/TDQ, PMMA/TCQ, and PMMA/TFQ are 540.41, 781.27, 977.13, and 822.55 MV m$^{-1}$, respectively. The corresponding Weibull shape parameters, which characterize the statistical dispersion of breakdown strength, are also presented in Figures S13–S15. After additive doping, Weibull breakdown curves shift toward higher electric fields, meaning the composites withstand larger fields at identical failure probability. PMMA/TCQ shows the most prominent shift to the high-field side, consistent with its lowest leakage current among the three composites. Lower conduction suppresses Joule heating during electrical stress and helps delay breakdown, although film defects and electrode contact conditions also influence final breakdown strength. Taken together, dielectric and high-field results separate two distinct behaviors. Low-field polarization responses change weakly upon doping, while charge transport and insulating capability vary dramatically depending on the substituted quinone additive. More importantly, the

consistent trends among the calculated molecular energy levels, TSDC-derived apparent trap characteristics, and experimentally measured leakage-current densities establish a clear correlation between quinone substituent chemistry and charge-transport regulation. These findings demonstrate that modifying the peripheral substituents of a common molecular framework provides an effective approach to tailoring high-field dielectric performance without relying on a substantial enhancement in dielectric permittivity.

### *3.3. Capacitive Energy-Storage Performance*

The suppressed leakage conduction and enhanced breakdown strength are favorable for capacitive energy storage. We therefore evaluated storage metrics including discharged energy density and charge–discharge efficiency at room temperature and 100 Hz (Figures 4a,b and S16–S20). As demonstrated by the concentration-dependent breakdown and energy-storage results in Figures S13–S18, an additive loading of 1.00 wt% was identified as the optimal composition for TDQ, TCQ, and TFQ based on their overall electrical performance. Accordingly, PMMA/TDQ-1.00, PMMA/TCQ-1.00, and PMMA/TFQ-1.00 were selected for the comparative analysis in the main text. For all samples, discharged energy density grows with applied electric field, while efficiency gradually declines. PMMA/TCQ retains the highest efficiency across most of the measured field window and tolerates the largest applied field, which translates into superior discharged energy density. At the maximum tested field, PMMA/TCQ achieves ~17.81 J cm$^{-3}$ while keeping efficiency above 80%.

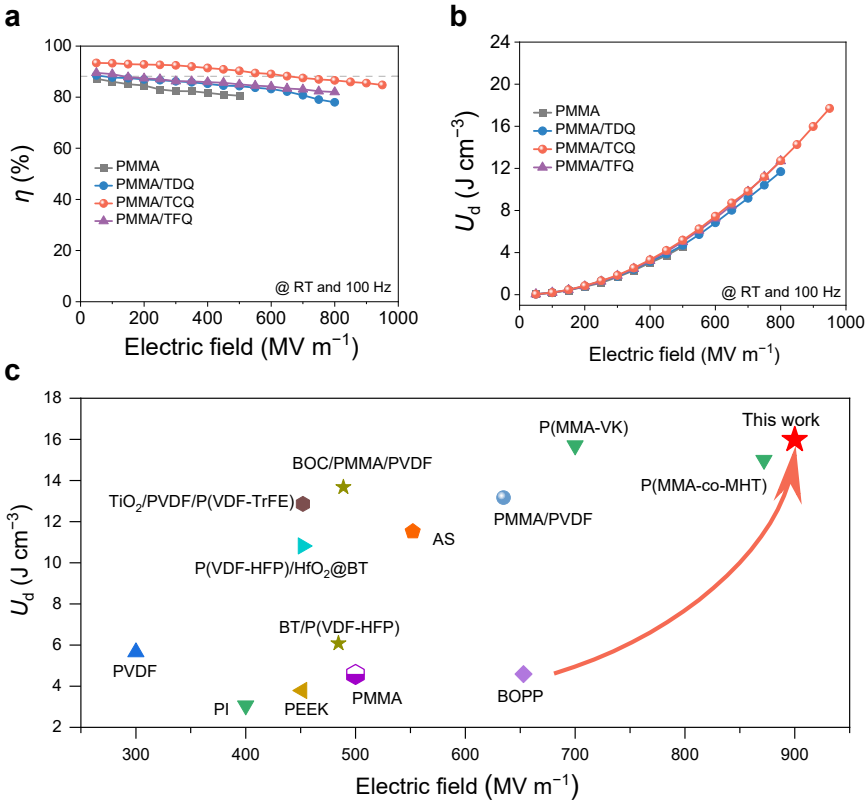



**Figure 4.** Energy storage performance and benchmark comparison of polymer dielectric films. (**a**) Charge–discharge efficiency as a function of applied electric field, measured at room temperature and 100 Hz; (**b**) discharge energy density as a function of applied electric field under the same test conditions; (**c**) comparison of discharge energy density of this work and previously reported polymer dielectric materials [4,7,19,20,34–42].

It is worth emphasizing that the composites show only minor differences in low-field permittivity, yet their energy storage performances diverge sharply. This highlights that

conduction loss and sustainable operating field serve as more decisive performance knobs. For near-linear dielectrics, stored energy scales with the square of electric field, so gains in high-field insulation deliver outsized benefits. Our work therefore demonstrates that rational molecular charge management can boost energy storage even when permittivity enhancement is modest.

The efficiency trend aligns with our earlier transport analysis. As the field increases, conduction loss introduces extra dissipation and reduces the fraction of energy recoverable during discharge. PMMA/TCQ combines minimal leakage current and high efficiency (Figure 4a), together with a shifted breakdown threshold that expands its usable field range (Figure 4b). These results collectively show that carrier confinement preserves efficient energy release and raises the maximum operational field.

Figure 4c benchmarks PMMA/TCQ against a selection of widely studied polymer dielectrics. PMMA/TCQ occupies the attractive high-field high-energy-density region and outperforms many previously reported systems. For instance, PVA-modified PMMA delivers 7.83 J $cm^{-3}$ at 580 MV $m^{-1}$ with an efficiency of 86.34%. By comparison, PMMA/TCQ reaches 17.81 J $cm^{-3}$ at 950 MV $m^{-1}$ with an efficiency of 84.08%. Although the measurement conditions vary among different studies, these results highlight the promising high-field energy-storage performance of PMMA/TCQ under the investigated conditions. This comparison underscores the competitiveness of our TCQ-doped PMMA composite for high-field capacitive energy storage.

### *3.4. Operational Reliability and Scalability Prospects*

Improved breakdown resistance also manifests as stable cycling reliability. PMMA/TCQ maintains steady performance over roughly $5 \times 10^4$ charge–discharge cycles at 400 MV $m^{-1}$ and room temperature. Under cycling conditions, its energy density stays near 3.2 J $cm^{-3}$ and efficiency remains above 90% (Figure 5a). *D–E* hysteresis loops collected at different cycle stages retain nearly identical shapes without obvious broadening (Figure 5b), so dissipative loss barely accumulates during cycling. In contrast, neat PMMA suffers from a more obvious decay in stored energy density over cycling.

We assessed spatial homogeneity by recording *D–E* loops at nine discrete locations across one PMMA/TCQ film with dimensions of 30 cm × 10 cm (300 $cm^2$). The nine measurement locations were distributed in a 3-by-3 arrangement, with three positions along each dimension, as illustrated in the inset of Figure 5c. The corresponding D–E loops are shown in Figure S21. Energy density hovers close to 3.2 J $cm^{-3}$ at all tested spots, and efficiency matches well across regions. Such spatial uniformity matters for practical dielectric films, because localized weak electrical spots often limit the performance of large-area devices. This result provides a solid foundation for future large-area fabrication trials.

Separately, we performed fast discharge measurements to characterize the pulse discharge capability of PMMA/TCQ (Figure 5d). At 200 MV $m^{-1}$ with a 100 kΩ load resistor, PMMA/TCQ releases ~0.87 J $cm^{-3}$, whereas commercial BOPP only outputs ~0.35 J $cm^{-3}$. The time required to release 90% of stored energy is ~10 μs for PMMA/TCQ and ~9.4 μs for BOPP. On comparable microsecond discharge timescales, PMMA/TCQ delivers around 2.5 times the energy density of BOPP, and its stored energy remains accessible within typical pulsed-power time windows.

Overall, cycling stability, spatial uniformity, and fast discharge data confirm that PMMA/TCQ exhibits reproducible storage response suitable for pulsed-power applications. The fully organic composition allows film fabrication via simple solution casting. This processing route offers convenient access to study how preparation parameters, film area, and thickness modulate performance uniformity in larger-scale specimens. Further investigations under prolonged electrical stress and elevated-temperature operating condi-

tions will be valuable for assessing device-level reliability and the long-term stability of the molecular additives.

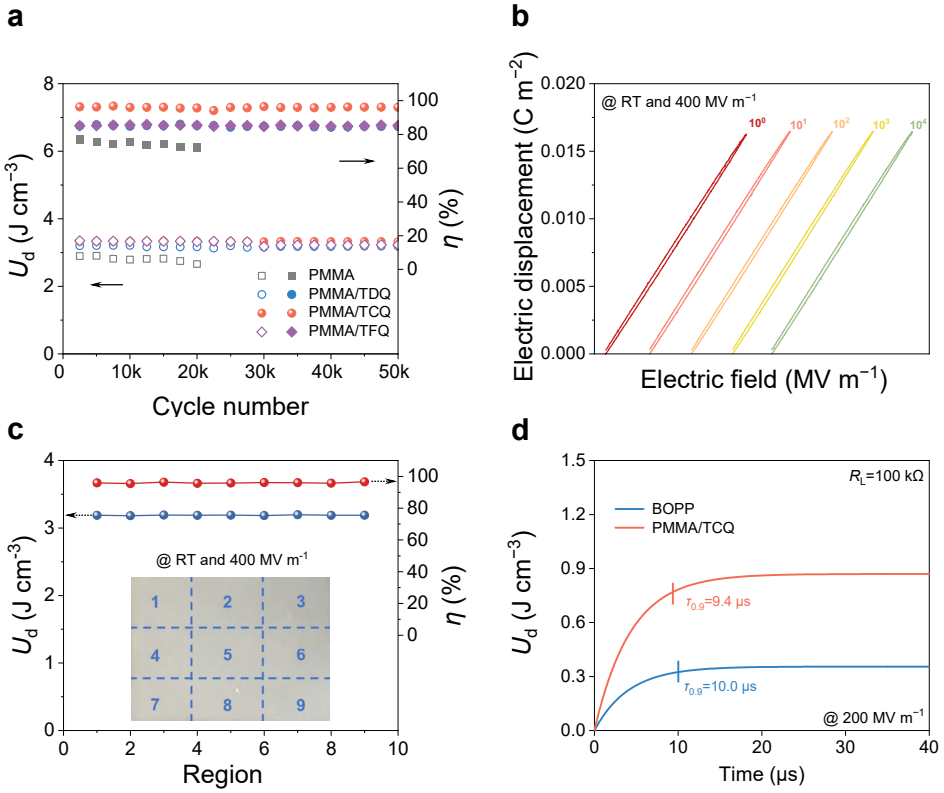



**Figure 5.** Cycling stability, *D*–*E* loop evolution during cycling, spatial uniformity, and discharge rate of composite dielectric films. (**a**) Discharge energy density and charge–discharge efficiency during 50,000 charge–discharge cycles at 400 MV m$^{-1}$ and room temperature; (**b**) electric displacement–electric field (*D*–*E*) loops recorded after 1, 10, 100, 1000, and 10,000 charge–discharge cycles; (**c**) spatial uniformity of discharge energy density and efficiency across 9 regions of the film, tested at 400 MV m$^{-1}$; (**d**) discharge speed comparison between PMMA/TCQ composite film and commercial BOPP film, measured at 200 MV m$^{-1}$ with a load resistance of 100 kΩ.

## 4. Conclusions

In summary, we report a substituent engineering strategy using quinone acceptors to construct controllable charge traps in PMMA dielectrics. Chlorine-substituted TCQ features deep LUMO levels and spatially confined electron-localization domains, which enable efficient electron capture and suppress long-range carrier migration. Theoretical calculations and TSDC results confirm that peripheral substitution regulates the energy-level alignment and electronic coupling between quinone additives and the PMMA matrix. Although the low-field permittivity only increases slightly upon doping, PMMA/TCQ exhibits greatly reduced leakage current and improved breakdown strength. Benefiting from this tailored charge-trapping effect, the composite achieves a discharged energy density of ~17.81 J cm$^{-3}$ with efficiency above 80%, alongside stable cycling performance, good spatial uniformity and fast microsecond discharge capability exceeding commercial BOPP. Different from conventional designs that pursue high permittivity, this work highlights molecular charge confinement as an effective route to boost high-field energy storage, and the all-organic, solution-processable system provides a transferable strategy for developing advanced polymer dielectrics toward pulsed-power applications. Beyond demonstrating the effectiveness of individual molecular trapping additives, this work provides a systematic understanding of how peripheral substitution within a common quinone framework

influences molecular electronic characteristics, charge-trapping behavior, and high-field dielectric performance, thereby offering a more specific molecular design basis for polymer capacitive energy storage.

**Supplementary Materials:** The following supporting information can be downloaded at https://www.mdpi.com/article/10.3390/chemistry8120166/s1. Figure S1. Electrostatic potential (ESP) distribution of the functional trap molecule. Histogram of normalized area fraction as a function of ESP; inset: ESP mapped on the molecular van der Waals surface (red for positive potential, blue for negative potential). Figure S2. FTIR spectra of pure PMMA and PMMA composite films doped with different quinone molecules. All spectra are vertically offset for clear comparison. Figure S3. Optical properties of pristine PMMA film. (a) UV–vis absorption spectrum recorded from 200 nm to 800 nm. (b) Tauc plot of $(\alpha h\nu)^2$ versus photon energy, with the optical band gap (Eg) determined by linear extrapolation. Figure S4. Optical properties of PMMA/TDQ composite film. (a) UV–vis absorption spectrum recorded from 200 nm to 800 nm. (b) Tauc plot of $(\alpha h\nu)^2$ versus photon energy, with a fitted optical band gap of 5.29 eV. Figure S5. Optical properties of PMMA/TCQ composite film. (a) UV–vis absorption spectrum recorded from 200 nm to 800 nm. (b) Tauc plot of $(\alpha h\nu)^2$ versus photon energy, with a fitted optical band gap of 5.23 eV. Figure S6. Optical properties of PMMA/TFQ composite film. (a) UV–vis absorption spectrum recorded from 200 nm to 800 nm. (b) Tauc plot of $(\alpha h\nu)^2$ versus photon energy, with a fitted optical band gap of 5.20 eV. Figure S7. Frequency-dependent dielectric properties of PMMA/TDQ composite films at room temperature. (a) Dielectric constant as a function of frequency ($10^2$–$10^6$ Hz). (b) Dielectric loss as a function of frequency ($10^2$–$10^6$ Hz). Figure S8. Frequency-dependent dielectric properties of PMMA/TFQ composite films at room temperature. (a) Dielectric constant as a function of frequency in the range of $10^2$–$10^6$ Hz. (b) Dielectric loss as a function of frequency in the range of $10^2$–$10^6$ Hz. Figure S9. Frequency-dependent dielectric properties of PMMA/TCQ composite films at room temperature. (a) Dielectric constant as a function of frequency in the range of $10^2$–$10^6$ Hz. (b) Dielectric loss as a function of frequency in the range of $10^2$–$10^6$ Hz. Figure S10. Temperature-dependent dielectric properties of PMMA/TDQ composite films at 1 kHz. (a) Dielectric constant in the temperature range of 30–100 °C. (b) Dielectric loss in the temperature range of 30–100 °C. Figure S11. Temperature-dependent dielectric properties of PMMA/TFQ composite films at 1 kHz. (a) Dielectric constant in the temperature range of 30–100 °C. (b) Dielectric loss in the temperature range of 30–100 °C. Figure S12. Temperature-dependent dielectric properties of PMMA/TCQ composite films at 1 kHz. (a) Dielectric constant in the temperature range of 30–100 °C. (b) Dielectric loss in the temperature range of 30–100 °C. Figure S13. Schottky and Poole–Frenkel analyses of leakage current in PMMA and PMMA/quinone composite films. (a) Schottky emission analysis; (b) Poole–Frenkel emission analysis. Symbols represent the experimental data, and solid lines represent the linear fitting results. Figure S14. Weibull statistical analysis of breakdown strength for PMMA/TCQ composite films. (a) Weibull distribution plots of breakdown field. (b) Characteristic breakdown field and shape parameter β of each sample. Figure S15. Weibull statistical analysis of breakdown strength for PMMA/4F composite films. (a) Weibull distribution plots of breakdown field. (b) Characteristic breakdown field and shape parameter β of each sample. Figure S16. Weibull statistical analysis of breakdown strength for PMMA/4$CH_3$ composite films. (a) Weibull distribution plots of breakdown field. (b) Characteristic breakdown field and shape parameter β of each sample. Figure S17. Energy storage performance of PMMA/4Cl composite films at room temperature and 100 Hz. Discharged energy density (left axis) and charge/discharge efficiency (right axis) as a function of applied electric field. Figure S18. Energy storage performance of PMMA/TDQ composite films at room temperature and 100 Hz. Discharged energy density (left axis) and charge/discharge efficiency (right axis) as a function of applied electric field. Figure S19. Energy storage performance of PMMA/TFQ composite films at room temperature and 100 Hz. Discharged energy density (left axis) and charge/discharge efficiency (right axis) as a function of applied electric field. Figure S20. Electric displacement-electric field ($D$–$E$) loops of PMMA/TCQ composite films with different doping ratios at 100 Hz and room temperature. Figure S21. Electric displacement-electric field ($D$–$E$) loops of PMMA/TDQ composite films with different doping ratios at 100 Hz and room temperature. Figure S22. Uniformity characterization of large-area composite film at room temperature and 400 MV $m^{-1}$. $D$–$E$ loops measured at 9 different regions of the large-area film.

**Author Contributions:** Conceptualization, Y.L.; methodology, Z.W. and Y.W.; validation, J.L. and Y.W.; formal analysis, Y.W. and X.G.; data curation, Y.W. and C.L.; writing—review and editing, Y.W. and Y.L.; project administration, Y.L.; supervision, Y.L.; funding acquisition, Y.L. All authors have read and agreed to the published version of the manuscript.

**Funding:** This research was supported by the National Natural Science Foundation of China (Grant Nos. 12274152 and 92366302) and the Guangdong Basic and Applied Basic Research Foundation (2024A1515010483) and received initial financial support from Huazhong University of Science and Technology. This work was also supported by the Guangdong Provincial Key Laboratory of Manufacturing Equipment Digitization (2023B1212060012).

**Data Availability Statement:** The original contributions presented in this study are included in the article/Supplementary Material. Further inquiries can be directed to the corresponding authors.

**Acknowledgments:** The authors would like to thank the Analytical and Testing Center of Huazhong University of Science and Technology for technical assistance.

**Conflicts of Interest:** The authors declare no conflicts of interest.

## References

1. Chen, J.; Zhou, Y.; Huang, X.; Yu, C.; Han, D.; Wang, A.; Zhu, Y.; Shi, K.; Kang, Q.; Li, P.; et al. Ladderphane Copolymers for High-Temperature Capacitive Energy Storage. *Nature* **2023**, *615*, 62–66. [CrossRef] [PubMed]
2. Wang, R.; Zhu, Y.; Fu, J.; Yang, M.; Ran, Z.; Li, J.; Li, M.; Hu, J.; He, J.; Li, Q. Designing Tailored Combinations of Structural Units in Polymer Dielectrics for High-Temperature Capacitive Energy Storage. *Nat. Commun.* **2023**, *14*, 2406. [CrossRef] [PubMed]
3. Wen, F.; Zhu, C.; Lv, W.; Wang, P.; Zhang, L.; Li, L.; Wang, G.; Wu, W.; Ying, Z.; Zheng, X.; et al. Improving the Energy Density and Efficiency of the Linear Polymer PMMA with a Double-Bond Fluoropolymer at Elevated Temperatures. *ACS Omega* **2021**, *6*, 35014–35022. [CrossRef] [PubMed]
4. Xie, J.; Liu, H.; Hu, J.; Zhao, X.; Song, S.; Sun, S.; Zhang, M. Solution-Processed Linear Methyl Methacrylate-Co-Glycidyl Methacrylate Films with Excellent Dielectric and Energy Storage Characters. *Mater. Adv.* **2022**, *3*, 6619–6627. [CrossRef]
5. Li, X.; Liu, B.; Wang, J.; Li, S.; Zhen, X.; Zhi, J.; Zou, J.; Li, B.; Shen, Z.; Zhang, X.; et al. High-Temperature Capacitive Energy Storage in Polymer Nanocomposites through Nanoconfinement. *Nat. Commun.* **2024**, *15*, 6655. [CrossRef] [PubMed]
6. Zhang, M.; Zhu, B.; Zhang, X.; Liu, Z.; Wei, X.; Zhang, Z. Depressing Relaxation and Conduction Loss of Polar Polymer Materials by Inserting Bulky Charge Traps for Superior Energy Storage Performance in High-Pulse Energy Storage Capacitor Applications. *Mater. Horiz.* **2023**, *10*, 2455–2463. [CrossRef] [PubMed]
7. Wang, T.; Zhang, M.; Song, R.; Fan, Z.; Mohamad, A.A.; Song, K.; Wang, D.; Zhang, M. Ultrahigh Energy Density in All-Organic Composites Synergistically Tailored by PMMA and Molecular Semiconductor. *Adv. Funct. Mater.* **2025**, *35*, 2422652. [CrossRef]
8. Chen, H.; Cui, Y.; Zou, G.; Liu, G.; Chen, C.; Wang, B.; Wu, T.; Shen, L.; Yan, S. High Breakdown and Energy Storage Properties of PMMA via Conformational Transition Induced by a Heat Treatment Strategy. *J. Phys. Chem. B* **2026**, *130*, 935–946. [CrossRef] [PubMed]
9. Gao, H.; Li, C.; Gong, Y.; Zhang, G.; Zhang, X.; Lu, J.; Zhou, H.; Liu, Y. Dielectric Polymers with Fluorinated-Moiety Clustering for High-Temperature Capacitive Energy Storage. *Energy Environ. Sci.* **2026**. [CrossRef]
10. Wang, Z.; Liu, J.; Gong, H.; Zhang, X.; Lu, J.; Zhang, Z. Synthesis of Poly(Methyl Methacrylate–Methallyl Alcohol) via Controllable Partial Hydrogenation of Poly(Methyl Methacrylate) towards High Pulse Energy Storage Capacitor Application. *RSC Adv.* **2016**, *6*, 34855–34865. [CrossRef]
11. Zhou, Y.; Zhu, Y.; Xu, W.; Wang, Q. Molecular Trap Engineering Enables Superior High-Temperature Capacitive Energy Storage Performance in All-Organic Composite at 200 °C. *Adv. Energy Mater.* **2023**, *13*, 2203961. [CrossRef]
12. Wan, Y.; Luo, H.; Yan, Z.; Shen, S.; Peng, J.; Li, X.; He, G.; Zhang, D.; Zha, J.-W. Decoupling Thermal Stability and Insulation in Dielectric Polymers via Donor-Acceptor Rearrangement. *Nat. Commun.* **2025**, *16*, 6242. [CrossRef] [PubMed]
13. Yang, T.; Wang, Y.; Li, C.; Shen, G.; Li, Y.; Huang, Z.; Zhang, Y.; Zhou, H.; Liu, Y. All-Organic Polybenzimidazole-Based Dielectrics for Capacitive Energy Storage at 250 °C. *J. Mater. Chem. A* **2026**, *14*, 43075–43085. [CrossRef]
14. Wang, Y.; Wu, H.; Chen, L.; Lin, S.; Li, C.; Zhang, Y.; Li, Y.; Zhou, H.; Liu, Y. Integrated Molecular Engineering Strategy in All-Organic Dielectrics for Ultrahigh-Temperature Capacitive Energy Storage. *Sci. China Mater.* **2026**, *69*, 5665–5672. [CrossRef]
15. Lin, S.; Wang, Y.; Wu, H.; Gao, X.; Li, C.; Liu, Y. Regulating Charge Transport in Polyetherimide via Small-Molecule Deep Traps for Efficient High-Temperature Energy Storage. *ACS Appl. Electron. Mater.* **2026**, *8*, 5619–5628. [CrossRef]
16. Zeng, T.; Meng, L.; Li, Q.; Liu, D.; Zhou, Q.; He, J.; Li, Q.; Yuan, C. Enhancing Energetic Disorder in All-Organic Composite Dielectrics for High-Temperature Capacitive Energy Storage. *Nat. Commun.* **2025**, *16*, 5620, Correction in *Nat. Commun.* **2025**, *16*, 7013. [CrossRef] [PubMed]

17. Zhang, Q.; Xie, Q.; Wang, T.; Huang, S.; Zhang, Q. Scalable All Polymer Dielectrics with Self-Assembled Nanoscale Multiboundary Exhibiting Superior High Temperature Capacitive Performance. *Nat. Commun.* **2024**, *15*, 9351. [CrossRef] [PubMed]
18. Yuan, C.; Zhou, Y.; Zhu, Y.; Liang, J.; Wang, S.; Peng, S.; Li, Y.; Cheng, S.; Yang, M.; Hu, J.; et al. Polymer/Molecular Semiconductor All-Organic Composites for High-Temperature Dielectric Energy Storage. *Nat. Commun.* **2020**, *11*, 3919. [CrossRef] [PubMed]
19. Zhang, M.; Zhu, B.; Zhang, X.; Tan, S.; Gong, H.; Wei, X.; Zhang, Z. High energy storage density and low energy loss achieved by inserting charge traps in all organic dielectric materials. *J. Mater. Chem. A* **2022**, *10*, 16258–16267. [CrossRef]
20. He, G.; Luo, H.; Yan, C.; Wan, Y.; Wu, D.; Luo, H.; Liu, Y.; Chen, S. Achieving synergistic improvement in dielectric and energy storage properties of all-organic poly(methyl methacrylate)-based copolymers via establishing charge traps. *Energy Environ. Mater.* **2024**, *7*, e12577. [CrossRef]
21. Cheng, Y.; Gong, H.; Zhang, M.; Ji, Q.; Zhang, G.; Zhang, X.; Zhang, Z. Overcoming energy storage-loss trade-offs in polymer dielectrics through the synergistic tuning of electronic effects in π-conjugated polystyrenes. *Adv. Sci.* **2025**, *12*, 2415738. [CrossRef] [PubMed]
22. Tang, X.; Ding, C.; Yu, S.; Zhong, C.; Luo, H.; Chen, S. Mechanism study of molecular trap in all-organic polystyrene-based dielectric composite. *Small* **2024**, *20*, 2306034. [CrossRef] [PubMed]
23. Zhao, Y.; Zhao, S.; Wu, S.; Zhang, M.; Yang, M.; Yang, L.; Ren, W.; Nan, C.-W.; Shen, Y. Optimizing traps and dihedral angles to modulate charge transport behavior for high-temperature dielectric energy storage. *Nat. Commun.* **2026**, *17*, 8418. [CrossRef] [PubMed]
24. Heinis, T.; Chowdhury, S.; Scott, S.L.; Kebarle, P. Electron affinities of benzo-, naphtho-, and anthraquinones determined from gas-phase equilibria measurements. *J. Am. Chem. Soc.* **1988**, *110*, 400–407. [CrossRef]
25. Li, C.; Gao, H.; Gong, Y.; Lin, Y.-T.; Liu, Y.; Wang, Y.; Chen, L.; Wu, H.; Cheng, L.; Li, Y.; et al. Ultrahigh High-Temperature Capacitive Energy Storage Via Proton Irradiation. *Adv. Sci.* **2026**, *13*, e22035. [CrossRef] [PubMed]
26. Gao, H.; Li, C.; Zhang, G.; Gong, Y.; Lin, S.; Li, Y.; Zhang, X.; Lu, J.; Zhou, H.; Liu, Y. All Organic PVDF-Based Polymer Composite for Capacitive Energy Storage Engineered via Structural Evolution. *npj Flex. Electron.* **2026**, *10*, 104. [CrossRef]
27. Gao, H.; Zhang, G.; Gong, Y.; Li, B.; Xu, Z.; Li, C.; Zhang, X.; Lu, J.; Zhou, H.; Liu, Y. Network-Structured All Organic Composite for High-Temperature Capacitive Energy Storage. *Adv. Energy Mater.* **2026**, *16*, e71395. [CrossRef]
28. Li, C.; Liu, Y.; Li, B.; Yuan, Z.; Yang, T.; Liu, Y.; Gao, H.; Xu, L.; Yu, X.; Luo, Q.; et al. Enhanced Energy Storage in High-Entropy Ferroelectric Polymers. *Nat. Mater.* **2025**, *24*, 1066–1073. [CrossRef] [PubMed]
29. Yu, X.; Li, C.; Li, L.; Yao, M.; Gao, H.; Liu, Y.; Yuan, Z.; Tang, S.; Luo, Q.; Zhang, H.; et al. Superb Energy Density in Biomass-Based Nanocomposites with Ultralow Loadings of Nanofillers. *J. Mater.* **2025**, *11*, 100960. [CrossRef]
30. Yu, X.; Li, L.; Gao, J.; Liu, Y.; Yuan, Z.; Yao, M.; Liu, Y.; Zhou, H. Ultra-High Energy Density in Cyanoethyl Biomass Polymers. *Adv. Funct. Mater.* **2024**, *34*, 2404613. [CrossRef]
31. Frisch, M.J.; Trucks, G.W.; Schlegel, H.B.; Scuseria, G.E.; Robb, M.A.; Cheeseman, J.R.; Scalmani, G.; Barone, V.; Mennucci, B.; Petersson, G.A.; et al. *Gaussian 09*; Gaussian, Inc.: Wallingford, CT, USA, 2009.
32. Hariharan, P.C.; Pople, J.A. Accuracy of $AH_n$ Equilibrium Geometries by Single Determinant Molecular Orbital Theory. *Mol. Phys.* **1974**, *27*, 209–214. [CrossRef]
33. Lu, T.; Chen, F. Multiwfn: A Multifunctional Wavefunction Analyzer. *J. Comput. Chem.* **2012**, *33*, 580–592. [CrossRef] [PubMed]
34. Hao, X.; Fu, Q.; Hou, Y.; Yan, Y.; Fu, T.; Cuan, J.; Du, P.; Luo, L.; Li, W. Enhancement of Energy Storage Performances in PMMA/PVDF Nanocomposites with Low Dielectric Bismuth Carbonate Nanosheets. *ACS Appl. Energy Mater.* **2022**, *5*, 15939–15947. [CrossRef]
35. Li, Q.; Tan, S.; Gong, H.; Lu, J.; Zhang, W.; Zhang, X.; Zhang, Z. Influence of Dipole and Intermolecular Interaction on the Tuning Dielectric and Energy Storage Properties of Polystyrene-Based Polymers. *Phys. Chem. Chem. Phys.* **2021**, *23*, 3856–3865. [CrossRef] [PubMed]
36. Lin, J.; Nie, L.; Yin, W.; Zhang, P.; Zuo, P.; Mi, P.; Zhuang, Q. Enhanced Dielectric Properties of Polyetherimide-Based Nanocomposite Films With Doped Semiconductor Traps. *Polym. Adv. Technol.* **2025**, *36*, e70127. [CrossRef]
37. Wang, G.; Huang, X.; Jiang, P. Mussel-Inspired Fluoro-Polydopamine Functionalization of Titanium Dioxide Nanowires for Polymer Nanocomposites with Significantly Enhanced Energy Storage Capability. *Sci. Rep.* **2017**, *7*, 43071. [CrossRef] [PubMed]
38. Wang, S.; Xu, P.; Xu, X.; Kang, D.; Chen, J.; Li, Z.; Huang, X. Tailoring the Electrical Energy Storage Capability of Dielectric Polymer Nanocomposites via Engineering of the Host–Guest Interface by Phosphonic Acids. *Molecules* **2022**, *27*, 7225. [CrossRef] [PubMed]
39. Liu, L.; Yun, H.; Chen, X.; Duan, Y.; Ji, Z.; Lv, S.; Zhang, Y. Preparation of Poly(Guaiacol Methacrylate-Methyl Methacrylate) Dielectric Films through Biobased Origin Guaiacol. *ACS Sustain. Chem. Eng.* **2024**, *12*, 2739–2750. [CrossRef]
40. Zheng, S.; Zhang, Z.; Lv, M.; Song, J.; Sun, S. Optimizing Cross-Linked Rigid-Flexible Structures to Enhance the Energy Storage Performance of Methyl Methacrylate-Co-Glycidyl Methacrylate at Elevated Temperatures. *Chem. Eng. J.* **2026**, *544*, 179152. [CrossRef]

41. Wang, S.; Zhang, Y.; Hao, G.; Wang, Y.; Gong, Z.; Zhang, C.; Zhang, Y.; Zhang, T.; Wang, Q. Excellent Energy Storage Performance of Multi-Alternating-Layer Structured PMMA/PVDF Dielectric Composite at High-Temperature. *Polymer* **2024**, *315*, 127772. [CrossRef]
42. Qiao, R.; Wang, C.; Chen, S.; He, G.; Liu, Z.; Luo, H.; Zhang, D. High-Temperature Dielectric Polymers with High Breakdown Strength and Energy Density via Constructing the Electron Traps in Blends. *Compos. Part A Appl. Sci. Manuf.* **2022**, *152*, 106679. [CrossRef]

**Disclaimer/Publisher's Note:** The statements, opinions and data contained in all publications are solely those of the individual author(s) and contributor(s) and not of MDPI and/or the editor(s). MDPI and/or the editor(s) disclaim responsibility for any injury to people or property resulting from any ideas, methods, instructions or products referred to in the content.